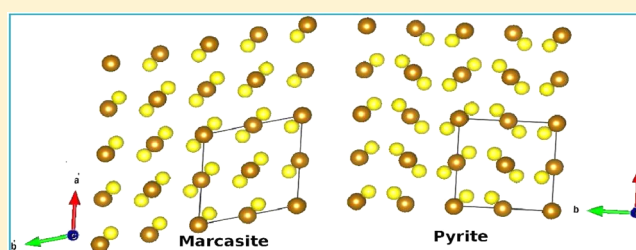


Phase Stability and Thermoelectric Properties of the Mineral FeS₂: An Ab Initio Study

Vijay Kumar Gudelli,[†] V. Kanchana,^{*,†} S. Appalakondaiah,[‡] G. Vaitheeswaran,[‡] and M. C. Valsakumar[§][†]Department of Physics, Indian Institute of Technology Hyderabad, Ordnance Factory Estate, Yeddumailaram-502 205, Andhra Pradesh, India[‡]Advanced Center of Research in High Energy Materials (ACRHEM), University of Hyderabad, Prof. C. R. Rao Road, Gachibowli, Hyderabad-500 046, Andhra Pradesh, India[§]School of Engineering Sciences and Technology (SEST), University of Hyderabad, Prof. C. R. Rao Road, Gachibowli, Hyderabad-500 046, Andhra Pradesh, India

ABSTRACT: First-principles calculations were carried out to study the phase stability and thermoelectric properties of the naturally occurring marcasite phase of FeS₂ at ambient conditions as well as under pressure. Two distinct density functional approaches were used to investigate these properties. The plane wave pseudopotential approach was used to study the phase stability and structural, elastic, and vibrational properties. The full potential linear augmented plane wave method has been used to study the electronic structure and thermoelectric properties. From the total energy calculations, it is clearly seen that marcasite FeS₂ is stable at ambient conditions, and it undergoes a first-order phase transition to pyrite FeS₂ at around 3.7 GPa with a volume collapse of about 3%. The calculated ground-state properties, such as lattice parameters, bond lengths, and bulk modulus of marcasite FeS₂, agree quite well with experimental values. In addition, phonon dispersion curves unambiguously indicated that the marcasite phase is stable under ambient conditions. Furthermore, we did not observe any phonon softening across the marcasite-to-pyrite transition. The possible reason for the transition was analyzed in the present study, which has not been attempted previously. In addition, we calculated the electronic structure and thermoelectric properties of both marcasite and pyrite FeS₂. We found a high thermopower for both phases, especially with p-type doping, which enabled us to predict that FeS₂ might have promising applications as a good thermoelectric material.



1. INTRODUCTION

Experimental and theoretical studies of iron-based sulphides have been of considerable interest in the last few decades in the geophysical context because of their occurrence on earth's surface and marine systems as well as on the surfaces of other planetary systems.¹ These compounds exhibit a wide range of interesting structural characteristics, such as epitaxial inter- and overgrowth of their polymorphic phases at lower temperatures. Also, they are found to exist in a variety of iron- or sulfur-deficient forms, which has implications for their mining and geochemical processing.^{2–9} Among the iron-based sulphides, FeS₂ is the most abundant natural mineral, and it is available in two closely related polymorphic structures, namely, marcasite and pyrite. Marcasite FeS₂ is the commonly available mineral in hydrothermal systems and in sedimentary rocks, whereas pyrite FeS₂ is the most abundant mineral on the earth's surface. Several works have investigated the similarities and differences between marcasite and pyrite crystal structures.^{10–12} In both structures, the Fe atoms are octahedrally coordinated with six S atoms and the S atoms are in tetrahedral coordination with three Fe atoms and one S atom. In detail, marcasite FeS₂ crystallizes in the orthorhombic structure (space group *Pnmm*, *Z* = 2) with Wyckoff position 2*a*(0,0,0) for Fe and 4*g*(*u*,*v*,0) for S.

The Sulfur octahedra, with which the Fe atoms are octahedrally coordinated, share the [110] edges (see the crystal structure in Figure 1a). On the other hand, pyrite FeS₂ crystallizes in a cubic structure (space group *Pa* $\bar{3}$, *Z* = 4) with Wyckoff position 4*a*(0,0,0) for Fe and 8*c*(*u*,*u*,*u*) for S. Thus, in the pyrite structure, the Fe atoms are situated at the corners and face centers, whereas the S atoms are placed in the form of S–S dumbbells oriented along the $\langle 111 \rangle$ directions with their centers at the body center and edge centers of the cube. A number of experiments have been performed on bulk pyrite and also on surfaces aiming to study the spectroscopic properties because of their potential applications in the photovoltaic industry.^{13–24} Jagadeesh and Seehra performed electrical resistivity measurements on natural marcasite, and its energy gap was found to be 0.34 eV.²⁵ The dynamical properties of these compounds have been measured by different experimental and theoretical methods.^{18,26–29} Apart from these experiments, several theoretical studies have also been carried out to explore the structural properties of FeS₂

Received: July 13, 2013

Revised: September 3, 2013

Published: September 11, 2013

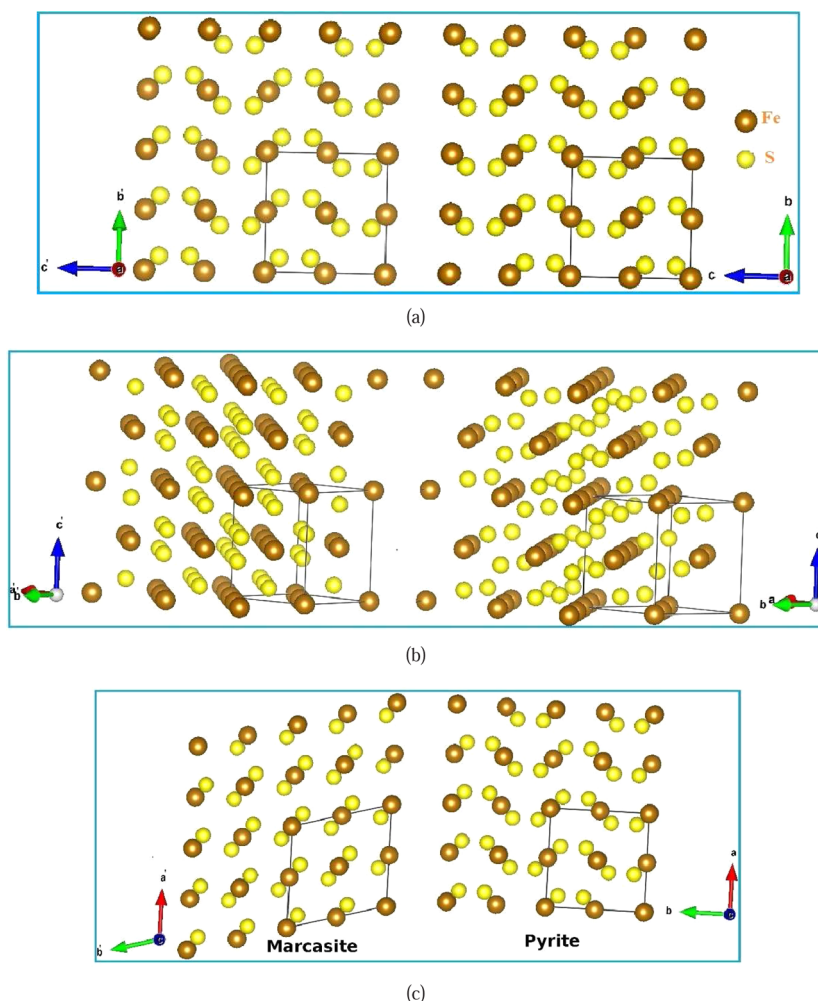


Figure 1. Marcasite supercell spanned by lattice translation vectors $\vec{a}' = \vec{a} + \vec{c}$, $\vec{b}' = -\vec{a} + \vec{c}$, and $\vec{c}' = \vec{b}$ compared with the conventional unit cell of pyrite. Here, \vec{a} , \vec{b} , and \vec{c} are the lattice translation vectors of the conventional unit cell of the marcasite structure. The (a) $\vec{b}' - \vec{c}'$ and (b) $\vec{a}' - \vec{c}'$ faces of the marcasite supercell are almost squares, whereas the (c) $\vec{a}' - \vec{b}'$ face of marcasite is a rhombus.

using combinations of density functional theory (DFT), Gaussian and plane wave basis sets, and all-electron and pseudopotential approaches. The mechanical properties of pyrite FeS_2 have been explored at different pressures using classical interatomic potentials, and marcasite is predicted to react in a manner similar to pyrite when compressed.³⁰ The electronic structure calculations for FeS_2 were performed using a nonempirical atomic orbital method, and the band gaps are reported for pyrite and marcasite forms of FeS_2 .³¹ Ahuja et al.³² have given a detailed discussion of the interband transitions in pyrite FeS_2 through optical properties. Merkal et al.³³ performed both experimental and theoretical investigations and concluded that cubic symmetry exists under high-pressure conditions.

Although numerous studies that analyze pyrite and marcasite from various perspectives are available, a precise study of both polymorphic forms of FeS_2 is needed to explain the phase stability of FeS_2 at ambient conditions. In the present work, we have studied both polymorphic forms of FeS_2 and have accounted for the first-order phase transition between marcasite and pyrite at high pressure and at zero temperature accompanied by a reasonable volume collapse which was not shown in any of the earlier studies; we have also speculated on the reasons driving the transition. Sun et al.³⁴ have also studied

the relative stability of FeS_2 with the aim of exploring the photovoltaic performance of FeS_2 . Similarly, it is also interesting to note that FeS_2 possesses a fairly good thermopower,³⁵ which previously has not been addressed theoretically. Thermoelectric (TE) materials have potential applications, including power generation and refrigeration, and have been a focus of research for experimentalists and theoreticians for the past few decades as they search for higher-performing materials. TE materials can convert waste heat into electric power; hence, they can play a vital role in mitigating the present energy crisis and environmental pollution.^{36,37} The performance of a TE material is quantified by the dimensionless figure of merit, ZT , which is given by

$$ZT = \frac{S^2 \sigma T}{\kappa}$$

where S , σ , T , κ are the Seebeck coefficient, electrical conductivity, absolute temperature, and thermal conductivity (which includes both the electronic κ_e and lattice contribution κ_l , that is, $\kappa = \kappa_e + \kappa_l$), respectively. It is clear that the value of ZT can be increased by making the values of thermopower and electrical conductivity high while keeping the value of thermal conductivity low. Assuming that the value of κ can be reduced to the amorphous limit, a way of maximizing ZT is to maximize

$S^2\sigma$. We have calculated for the first time the thermoelectric properties of FeS_2 in both polymorphic phases from this perspective.

The rest of the paper is organized as follows: In Method of Calculations, we describe the method used for the theoretical calculations. Structural properties are presented in Results and Discussion. In Electronic and Thermoelectric Properties, we discuss the electronic structure and thermoelectric properties. The Conclusion includes a summary of our findings.

2. METHOD OF CALCULATIONS

All the total energy calculations were performed using a plane wave self-consistent field program (Pwscf) based on density functional theory, a plane wave basis set, and a pseudopotential method.³⁸ The total energies are obtained by solving the Kohn–Sham equation self-consistently within the generalized gradient approximation (GGA) of the Perdew–Burke–Ernzerhof (PBE) potential.³⁹ A plane wave kinetic energy cutoff of 50 Ry is used, and the first Brillouin zone is sampled according to the Monkhorst–Pack scheme⁴⁰ by means of a $8 \times 8 \times 8$ k-mesh to ensure well-converged results. The electron–ion interactions are described by Vanderbilt-type ultrasoft pseudopotentials,⁴¹ and the pseudopotentials are treated with nonlinear core corrections with the following basis set as valence states: Fe, $3s^23p^63d^64s^2$ and S, $3s^23p^4$. The variable-cell structural optimization has been performed using the Broyden–Fletcher–Goldfarb–Shanno (BFGS) algorithm as implemented in Pwscf. To obtain information about the relative phase stability of marcasite and pyrite phases as a function of pressure, we have calculated the cohesive energy of both the phases at pressures ranging from -3 GPa (expansion) to 9 GPa (compression) with a step size of 0.5 GPa. For each pressure, structural optimization of the unit cell has been carried out by relaxing positions of all the atoms together with the necessary changes in the shape and volume. The threshold criteria of 1×10^{-5} Ry for total energies, 1×10^{-4} Ry/bohr for the maximum force, and 0.002 GPa for total stress were used for the structural relaxation. The phonon dispersion calculations are performed within the framework of density functional perturbation theory (DFPT). Dynamical matrices were set up and diagonalized for phonon wavevectors corresponding to a Monkhorst–Pack grid of $4 \times 4 \times 4$. To calculate the elastic properties of FeS_2 , we have used the CASTEP package,^{42,43} which is also based on the plane wave pseudopotential method. To obtain well-converged parameters, we have used a plane wave cutoff of 800 eV and a Monkhorst–Pack⁴⁰ grid with a minimum spacing of 0.025 \AA^{-1} using GGA–PBE exchange–correlation functional with ultrasoft pseudopotential. The elastic constants can be computed by calculating the elastic energy as a function of elastic strain. More specifically, the curvature of the elastic energy as a function of a value of a particular type of elastic strain gives the value of a particular combination of elastic constants. By repeating the calculations for an adequate number of independent strains, we can obtain the required number of independent equations for the elastic constants which can be solved to obtain the values of the independent elastic constants. For each strain, the coordinates of the ions are fully relaxed, keeping intact the shape of the unit cell corresponding to the given strain. After obtaining the single-crystal elastic constants, we have calculated polycrystalline properties such as the bulk modulus, shear modulus, sound velocities, and Debye temperature using the Voigt–Ruess–Hill (VRH)⁴⁴ approximation

(see Ravindran et al.⁴⁵ for a detailed discussion on these calculations).

To study the electronic properties, we have used the full-potential linear augmented plane wave (FP-LAPW) method based on first-principles density functional calculations as implemented in WIEN2k.⁴⁶ It is well-known that for semiconductors and insulators the electronic band gap calculated using DFT with standard exchange–correlation functionals, such as LDA and GGA, is usually about 30–40% less than that found by experiment because of self-interaction and the lack of derivative discontinuities of the exchange correction potential with respect to occupation number.^{47,48} In the present work, we have used a modified GGA, known as Tran and Blaha modified Becke–Johnson potential (TB-mBJ),⁴⁹ which is found to be quite successful in reproducing the experimental band gaps as compared to those found using standard GGA.^{48,50–53} Here we have used $9 \times 8 \times 12$ and $15 \times 15 \times 15$ Monkhorst–Pack k-meshes for the self-consistent calculations, resulting in 175 and 176 k-points in the irreducible part of the Brillouin zone, respectively, for the marcasite and pyrite phases. Spin–orbit coupling has been incorporated in our calculations. All our calculations are performed using the optimized parameters from the Pwscf calculation with an energy convergence up to 10^{-6} Ry per unit cell between the successive iterations. Furthermore, we have calculated the thermopower (S) and σ/τ using the BOLTZTRAP⁵⁴ code with well-converged parameters (using as many as 100 000 k-points in the Brillouin zone) using the self-consistent calculation within the rigid band approximation (RBA)^{55,56} and the constant scattering time (τ) approximation (CSTA). According to the RBA approximation, doping a system does not vary its band structure but varies only the chemical potential. The RBA is a good approximation to calculate the transport properties for doped semiconductors when the doping level is not very high.^{56–60} According to the CSTA, the scattering time of the electron is independent of energy and depends on concentration and temperature. A detailed explanation about the CSTA is given in refs 61–63 and the references therein. It is evident that CSTA has been quite successful in predicting the thermoelectric properties of many materials.^{64–66}

3. RESULTS AND DISCUSSION

3.1. Phase Stability of FeS_2 . The structural phase stability of the marcasite and pyrite phases of FeS_2 has been studied to find the ground state of FeS_2 at various pressures. As a first step, we have performed total energy calculations as a function of volume for both marcasite and pyrite FeS_2 structures by varying pressures from -3 to 9 GPa. Here, the negative and positive pressures represent expansion and compression of the unit cell, respectively. As shown in Figure 2, the total energy curves clearly show marcasite is energetically favored over pyrite with an energy difference of ~ 0.03 Ry/atom. A similar result has been obtained by a recent study on FeS_2 using a different numerical implementation.¹⁸ Even though similar studies exist in the literature, none of them clearly identified marcasite as the ground state of the polymorphic FeS_2 . From Figure 2, we found a possible structural phase transition from marcasite to pyrite FeS_2 at a V/V_0 value of ~ 0.98 , where V is the theoretical volume and V_0 is the experimental volume. To obtain the transition pressure, we have also plotted the enthalpy difference versus pressure (Figure 3a). From this plot, the pressure for the marcasite-to-pyrite phase transition is determined to be 3.7 GPa. As shown in Figure 3b, there is a volume collapse of $\sim 3\%$,

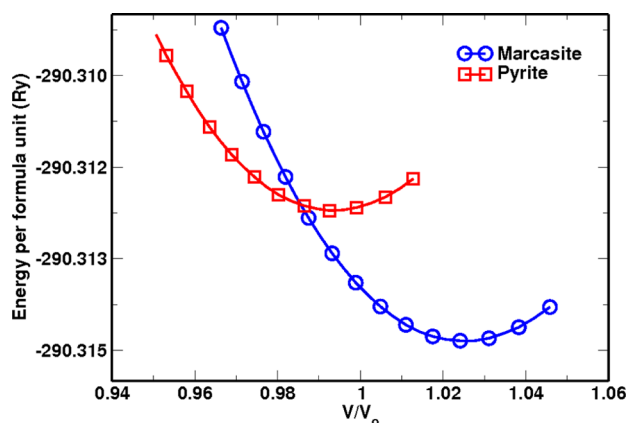


Figure 2. Total energy curves as a function of relative volume for FeS_2 ; circles and squares represents marcasite and pyrite, respectively.

which indicates the first-order character of the phase transition from the marcasite to pyrite structure. In the present study we specifically address the ground-state as well as high-pressure properties of marcasite FeS_2 , which was not reported previously. It is interesting to note that there are no conspicuous signatures of the marcasite-to-pyrite transition in the phonon dispersion, Raman, or IR spectra of marcasite FeS_2 at ambient or high pressures. We shall discuss this in more detail in later sections.

3.2. Structural Properties. The calculated structural properties, such as lattice constants, volume, internal parameters (u and ν) of sulfur, and bond lengths of Fe–Fe, Fe–S, and S–S for marcasite FeS_2 , are compared with experimental and other theoretical reports and are summarized in Table 1. The calculated lattice parameters and volume are in reasonable agreement with the calculations of Spagnoli et al.¹⁸ and Sithole et al.⁶⁹ The minor differences found when compared to the results of Sithole et al.⁶⁹ are due to different parametrizations of the exchange–correlation functional used in their calculations.

The relative change of lattice parameters a , b , and c with respect to external pressure up to 5 GPa are shown in Figure 4a. We found that marcasite FeS_2 is relatively less compressible along the b -direction than it is along the a - and c -directions. The pressure coefficients

Table 1. Ground-State Properties of Marcasite FeS_2 at Ambient Pressure Compared with Other Experimental and Theoretical Reports

parameters	present work	experimental	results from other calculations
a (Å)	4.439	4.436 ^a	4.434 ^c , 4.373 ^d
b (Å)	5.408	5.414 ^a	5.404 ^c , 5.381 ^d
c (Å)	3.388	3.381 ^a	3.387 ^c , 3.407 ^d
u (S)	0.206	0.200 ^a	0.203 ^d
ν (S)	0.375	0.378 ^a	0.380 ^d
V (Å ³)	81.33	81.20 ^a	81.16 ^c , 80.17 ^d
B_0 (GPa)	150.1	146.5 ^b	
B'	5.4	4.9 ^b	
Fe–Fe (Å)	3.38	3.36 ^a	3.386 ^d
Fe–S (Å)	2.23	2.21 ^a	2.229 ^d
S–S (Å)	2.20	2.19 ^a	2.195 ^d

^aRef 67. ^bRef 68. ^cRef 18. ^dRef 69.

$$y(x) = \left. \frac{1}{x} \frac{dx}{dP} \right|_{P=0}$$

(where x is a , b , or c) of the lattice parameters are found to be 2.2×10^{-3} , 1.8×10^{-3} , and 1.9×10^{-3} GPa, respectively. This means that $y(b) < y(c) < y(a)$, implying least compressibility is along the b -axis. The Fe–S_{*i*} ($i = 1, 2$) bond lengths monotonically decrease with pressure (Figure 4b). The variation of fractional coordinates (u and ν) of sulfur as a function of pressure is found to be less significant. Overall, the structural parameters of marcasite FeS_2 show minor changes under pressure, which implies that marcasite FeS_2 shows almost isotropic behavior with external pressure despite crystallizing in an orthorhombic structure. The bulk modulus (B_0) and its pressure derivative (B'), calculated using the Birch–Murnaghan equation of state, are 150.1 GPa and 5.7, respectively, for marcasite FeS_2 , which are in good agreement with the earlier experimental values of 146.5 GPa and 4.9, respectively.⁶⁸

3.3. Mechanical Properties. To obtain the mechanical stability of marcasite type FeS_2 , we have calculated elastic properties of this material. Elastic constants are the fundamental material parameters that describe the resistance of the material against applied mechanical deformation. Because marcasite FeS_2 crystallizes in an orthorhombic structure, it has nine independent elastic constants, namely, C_{11} , C_{22} , C_{33} , C_{44} ,

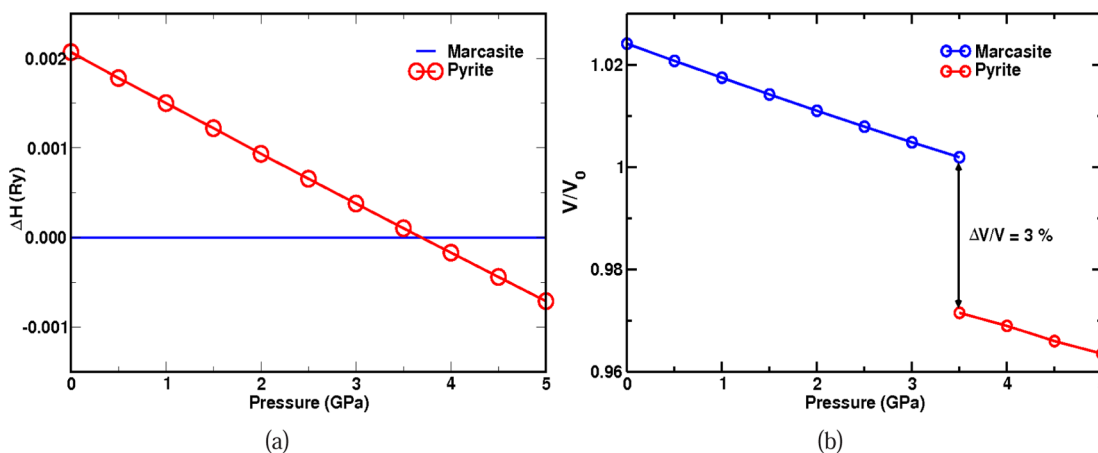


Figure 3. Phase transition from marcasite to pyrite per unit cell. (a) Change in enthalpy and (b) Corresponding volume collapse with respect to the pressure.

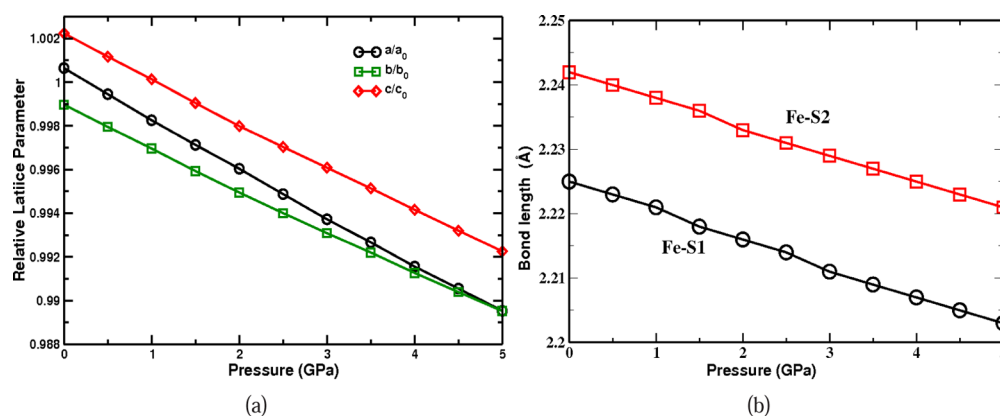


Figure 4. Evolution of structural properties of marcasite with pressure up to 5 GPa. (a) Relative lattice parameters and (b) Bond lengths.

Table 2. Single-Crystal Elastic Constants (C_{ij} , GPa), Bulk Moduli (B_X , $X = V, R, \text{ or } H$), Shear Moduli (G_X , $X = V, R, \text{ or } H$) and Sound Velocities (v_l, v_t, v_m , km/sec) and Debye Temperature ($\Theta(D)$, K) of FeS_2 ^a

C_{11}	C_{22}	C_{33}	C_{44}	C_{55}	C_{66}	C_{12}	C_{13}	C_{23}	
303.1	454.3	322.8	105.9	158.2	153.9	47.0	106.4	55.8	
B_V	B_R	B_H	G_V	G_R	G_H	v_l	v_t	v_m	$\Theta(D)$
166.5	164.8	165.7	141.7	133.9	137.8	8.35	5.25	5.78	634.9

^aAll quantities are calculated at the respective theoretical equilibrium volume obtained with the PBE functional.

C_{55} , C_{66} , C_{12} , C_{13} , and C_{23} . To calculate the elastic constants, we have performed complete structural optimization of the experimental structure using CASTEP. The calculated single-crystal elastic constants at the theoretical equilibrium volume are tabulated in Table 2. All the calculated single-crystal elastic constants satisfied the Born's mechanical stability criteria for orthorhombic structure,⁷⁰ thereby implying that the marcasite type FeS_2 is mechanically stable under ambient conditions. From the calculated values it is clearly observed that $C_{22} > C_{33} > C_{11}$, which implies that marcasite FeS_2 is stiffer along the b -direction than along the \bar{c} - and \bar{a} - directions. The single-crystal bulk modulus calculated from elastic constants is 164.8 GPa, which is in reasonable agreement with the 150.1 GPa value obtained in this work using the Birch–Murnaghan equation of state. By using the calculated single-crystal elastic constants, we further computed the polycrystalline aggregate properties such as bulk moduli (B_X , $X = V, R, \text{ or } H$), shear moduli (G_X , $X = V, R, \text{ or } H$) using the Voigt, Reuss, and Hill approaches. The calculated polycrystalline bulk modulus for marcasite type FeS_2 is 165.7 GPa from single-crystal elastic constants, which is in reasonable agreement with the single-crystal bulk modulus. It is seen that $B_H > G_H$ for polycrystalline FeS_2 , which implies that the quantity that limits mechanical stability is G_H . Apart from these, we also calculated the Debye temperature ($\Theta(D)$) using sound velocities. $\Theta(D)$ is a fundamental quantity that correlates several physical properties such as specific heat, thermal conductivity, and melting point of the crystal with elastic constants. At low temperatures, $\Theta(D)$ can be estimated from the average sound velocity (v_m), which is the average of longitudinal (v_l) and transverse (v_t) sound velocities. The calculated values of v_l , v_t , v_m and $\Theta(D)$ are shown in Table 2. This is the first qualitative prediction of the mechanical properties of marcasite type FeS_2 .

3.4. Phonon Dispersion and Zone-Centered Frequencies. We have studied the phonon dispersion of marcasite FeS_2 as a function of pressure from ambient conditions to 5 GPa using DFPT.⁷¹ Because instability of one or more phonon

modes would be indicative of dynamical instability of the structure, we have carried out the study of phonon dispersion in the entire first Brillouin zone to investigate the dynamic stability of the marcasite structure. The unit cell of marcasite FeS_2 contains 6 atoms; hence, it has 18 phonon modes for each wavevector, out of which three are acoustic and the remaining 15 modes are optical modes. According to the group theoretical analysis, the optical modes at Γ -point can be represented as

$$\Gamma = 2A_g + 2B_{1g} + B_{2g} + B_{3g} + 2A_u + B_{1u} + 3B_{2u} + 3B_{3u} \quad (1)$$

In this analysis, the A_u mode is inactive, whereas the modes A_g , B_{1g} , B_{2g} , and B_{3g} are Raman active and B_{1u} , B_{2u} , and B_{3u} modes are infrared active. The calculated zone center frequencies at ambient pressure are shown in Table 3 accompanied by experimental and other theoretical results. The calculated values are in reasonable agreement with experiment. In an earlier study, Spangnoli et al.¹⁸ reported the zone center frequencies for both pyrite and marcasite structures, and their results show both the structures have zone centered modes with real frequencies, implying stability of the modes. We also find a similar situation in our case. We have also calculated zone center frequencies as a function of pressure, and we observe no imaginary frequencies at zone center. The calculated zone-centered vibrational frequencies up to 5 GPa are shown in Figure 5a. From this figure it is clear that there is no softening of zone-centered frequencies, and it allows us to confirm that marcasite is dynamically stable up to 5 GPa.⁷² It is to be emphasized that there are no signatures of the impending pressure-induced structural phase transition in the phonon spectra. In addition, the calculated dispersion curves along high-symmetry directions and the corresponding phonon density of states for marcasite FeS_2 at $P = 0$ GPa and $P = 4$ GPa are shown in Figure 5b. There is considerable overlap between the acoustic and optical modes, which can be clearly seen from the phonon dispersion. The optical mode frequencies from 310 to

Table 3. Comparison of Present Calculated Phonon Frequencies with Experimental and Other Theoretical Vibrational Frequencies (cm^{-1}) of Marcasite FeS_2 at 0 GPa

mode	present work	experimental ^a	theoretical ^b
A_u	202.64	inactive	207
B_{2u}	248.82	325	248
B_{3u}	288.64	293	279
A_g	305.23	323	317
B_{2u}	317.95	404	323
B_{3g}	320.20	367	339
B_{2g}	322.60	308	342
B_{3u}	361.90	353	360
A_u	366.57		
B_{3u}	367.76	387	373
A_g	377.43	386	388
B_{1g}	379.25	377	382
B_{2u}	392.13	432	385
B_{1u}	399.79	404	409
B_{1g}	456.56	455	

^aRef 27. ^bRef 18.

390 cm^{-1} are dominated by S atoms. We do not find any imaginary phonon frequencies in the phonon dispersion curves along any direction of the Brillouin zone at ambient or high

pressure. This clearly establishes the dynamical stability of marcasite FeS_2 . However, because linear response theory is based on harmonic approximation, anharmonic effects are ignored in the present calculations. It is plausible that anharmonic effects may also play a role in driving the observed structural phase transition. We have also calculated Raman and IR spectra of marcasite FeS_2 from ambient pressure to 5 GPa. From this, we found that Raman peak intensities decrease with increasing pressure, whereas IR peak intensities increase with increasing pressure. However, the peaks are shifted to higher frequencies in both cases. The calculated IR and Raman spectra at ambient and 5 GPa are shown in Figure 5c,d.

3.5. Transition from Marcasite to Pyrite. On the basis of the total energy calculations of marcasite and pyrite FeS_2 shown in Figure 2, we infer the possibility of a structural phase transition from ground-state marcasite to the pyrite structure. It is also worth noting that earlier experiments found pyrite to exist only at high pressures.^{14,33} Interestingly, we did not observe any phonon softening or structural variations in marcasite FeS_2 by our calculations under pressure. Generally, most of the MX_2 type compounds crystallize in pyrite, marcasite, or arsenopyrite structures. These structures are closely related to each other.⁷³ Marcasite structure is further classified into *regular marcasite* and *anomalous marcasite* depending on the c/a ratio and bond angle (M–X–M)

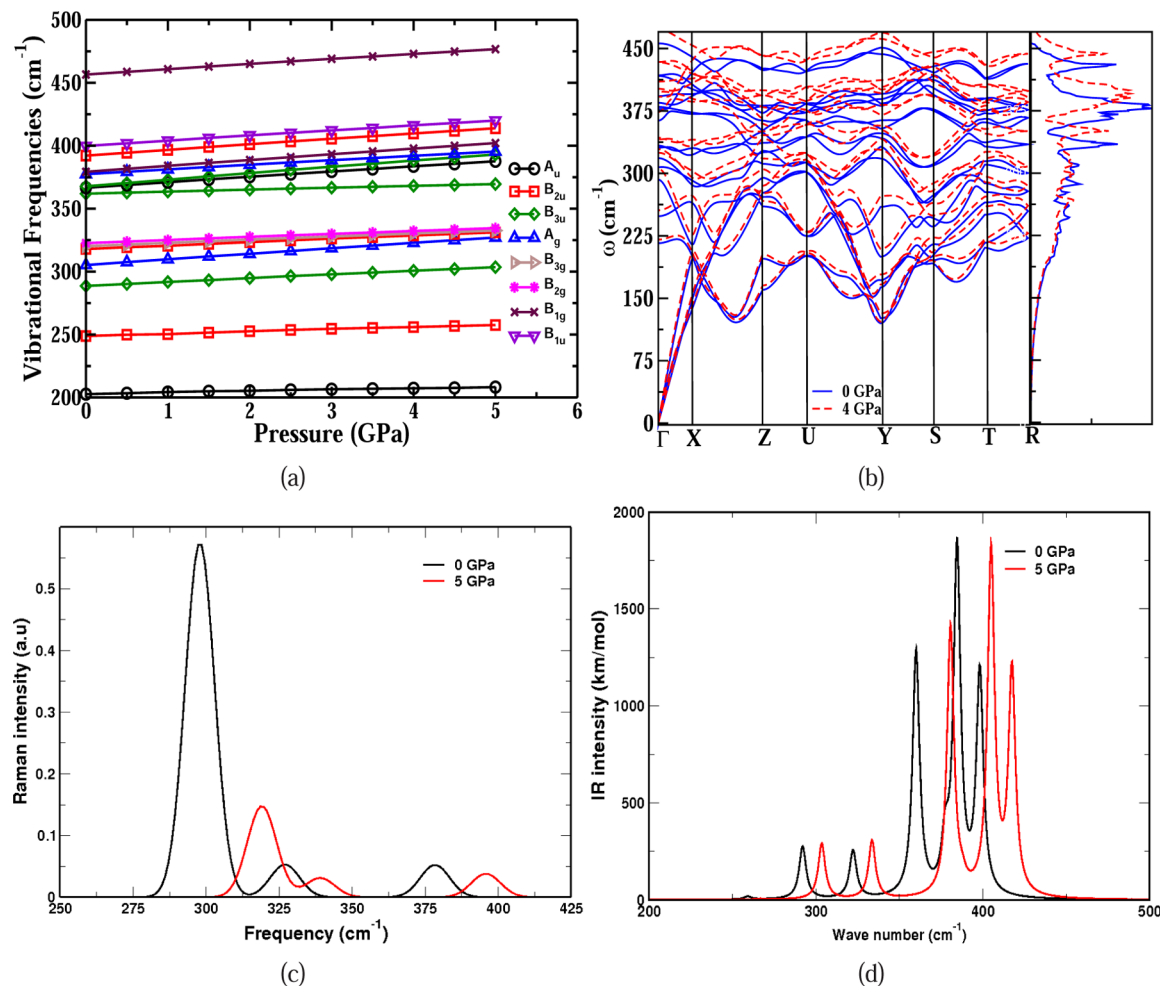


Figure 5. Vibrational properties of marcasite FeS_2 . (a) Zone-centered vibrational frequencies from 0 to 5 GPa (b) Phonon dispersion along high-symmetry directions and total phonon density of states at 0 and 4 GPa (c) Raman spectra at 0 and 5 GPa, and (d) IR spectra at 0 and 5 GPa.

between neighboring cations in the edge-shared octahedra. A c/a ratio around 0.53–0.57 and bond angle less than 90° correspond to regular marcasite, whereas anomalous marcasite has a c/a ratio of 0.73–0.75 and a bond angle greater than 90° . In the present study, the calculated c/a ratio and bond angle for marcasite FeS_2 are found to be 0.76 and 98.6° , respectively. From this it is clear that FeS_2 belongs to the class of anomalous marcasite.

We now proceed to describe the mechanism that drives the marcasite-to-pyrite transition under hydrostatic pressure. The similarities and differences between the two competing structures are quite evident when the marcasite supercell spanned by lattice translation vectors $\vec{a}' = \vec{a} + \vec{c}$, $\vec{b}' = -\vec{a} + \vec{c}$, and $\vec{c}' = \vec{b}$ is compared with the conventional unit cell of pyrite (Figure 1a–c). Here, \vec{a} , \vec{b} , and \vec{c} are the lattice translation vectors of the conventional unit cell of the marcasite structure. Both cells contain the same number of atoms. The Fe atoms and the centers of the S_2 dimers have the same fractional coordinates in both cells. While all faces of the pyrite unit cell are squares, the $\vec{a}' - \vec{c}'$ and $\vec{b}' - \vec{c}'$ faces of the marcasite supercell are almost squares, whereas the $\vec{a}' - \vec{b}'$ face of the marcasite is a rhombus with a 105.37° angle between \vec{a}' and \vec{b}' . Furthermore, while the orientation of the S_2 dimers with centers lying on lines parallel to the \vec{a}' direction of marcasite cell are the same, it flips by $\pi/2$ along alternate lines in the pyrite structure. In the present calculation we found that the marcasite structure is most compressible along \vec{a} , less compressible along \vec{c} and least compressible along b -direction. Therefore when a sufficiently large hydrostatic pressure is applied, there is a differential compression along \vec{a} as compared to the \vec{c} -direction of marcasite cell. This results in reducing the angle between \vec{a}' and \vec{b}' . When the pressure is increased further, this differential change can trigger a flipping of the S_2 dimers along alternate lines parallel to \vec{a}' direction by $\pi/2$, thereby facilitating a discontinuous transformation of the rhombus into a square. This, together with relaxation of atomic positions, leads to the marcasite-to-pyrite transformation.

4. ELECTRONIC AND THERMOELECTRIC PROPERTIES

4.1. Band Structure and Density of States. Quite a good number of electronic structure calculations are reported in the literature aimed at understanding the band structure and density of states of both marcasite and pyrite structures. It is well-known that the thermoelectric properties are quite sensitive to the details of the band structure. It is therefore clear that the reliability of the computed thermoelectric properties would depend on the accuracy of the electronic structure calculations. From this perspective, we have repeated the band structure and density of state calculations using TB-mBJ potential, which is well-known to reproduce accurately the experimental band gap values.^{48,50–53} The calculated band structure for both orthorhombic marcasite at 0 GPa and cubic pyrite at 4 GPa along the high-symmetry directions of the Brillouin zones (see Figure 6a,b) are shown in Figure 7a,b. From the band structure analysis, we have seen that the conduction band minimum (CBM) and valence band maximum (VBM) are located at two different high-symmetry points in the Brillouin zone, making the material an indirect band gap semiconductor in both structures. The calculated band gap of marcasite is found to be 1.603 eV, and in pyrite it is 1.186 eV. In the case of marcasite, we predict the band gap to be much higher than the experimental band gap of 0.34 eV²⁵ obtained from resistivity measurement. It must be mentioned

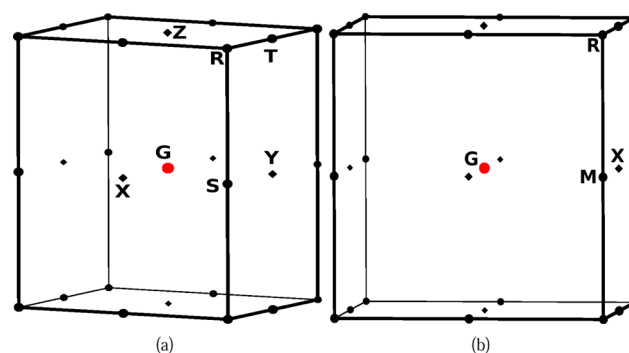


Figure 6. Brillouin zone of (a) Marcasite and (b) Pyrite.

that this observation is similar to the results obtained using other exchange–correlation functions.³⁴ In the case of pyrite, there is a wide range of reported band gap values, from 0.7 to 2.62 eV,^{14,15,31,74–78} and this spread in values of the energy gap may be due to the experimental limitations as mentioned by Ennaoui et al. and Ferrer et al.^{14,15} The photoconductivity measurements show a consistent band gap for the pyrite in the range of 0.9–0.95 eV, which is in good agreement with the optical and conductivity experiments.^{14,77} This value is also in good agreement with our present calculations and the recent calculations performed by Hu et al.⁷⁸ We also investigated dependence of the value of band gap on the position of S atoms in the marcasite unit cell. Unlike the extreme sensitivity of E_g seen in earlier calculations for the pyrite structure,⁷⁹ we did not find any significant variation in the band gap of marcasite with position of S atoms. From the band structure analysis, we find that the CBM is located between Γ and X points in the Brillouin zone, whereas in the case of pyrite we find it at the center of the Brillouin zone. The VBM in the case of marcasite is located along the Γ –Y direction with a highly dispersed band, whereas in the case of pyrite it is clearly seen at the X point with less dispersion toward the Γ point. These bands mainly arise from the Fe d and S p states in both structures, but in the case of marcasite, the contribution of these states is low compared to that of the pyrite. The principal aim of the present work is to calculate the thermoelectric properties of FeS_2 and its variation with carrier concentration. It is necessary to estimate the effective masses of the carriers in various electron and hole pockets to achieve this task. We have calculated the mean effective mass of the carriers at the conduction and valence band edges by fitting the energy of the respective bands to a quadratic polynomial in the reciprocal lattice vector \vec{k} . The calculated effective masses for both marcasite and pyrite structures in some selective directions of the Brillouin zone are tabulated in Table 4. It is quite clear that the bands are less dispersive in the pyrite structure in almost all of the high-symmetry directions. This would imply large effective mass for the carriers belonging to these bands and hence a high thermopower. However, presence of carriers with large mobility is required for obtaining a higher electrical conductivity. Thus, there is a possibility of obtaining large a ZT factor in materials possessing multiple pockets of carriers with large and small effective masses; the former leads to large S, and the latter enhances σ .^{63,64} It is interesting to note that the electronic structure of both phases of FeS_2 reveals the presence of multiple carrier pockets with substantially different effective masses, suggesting that they may have good thermoelectric properties.

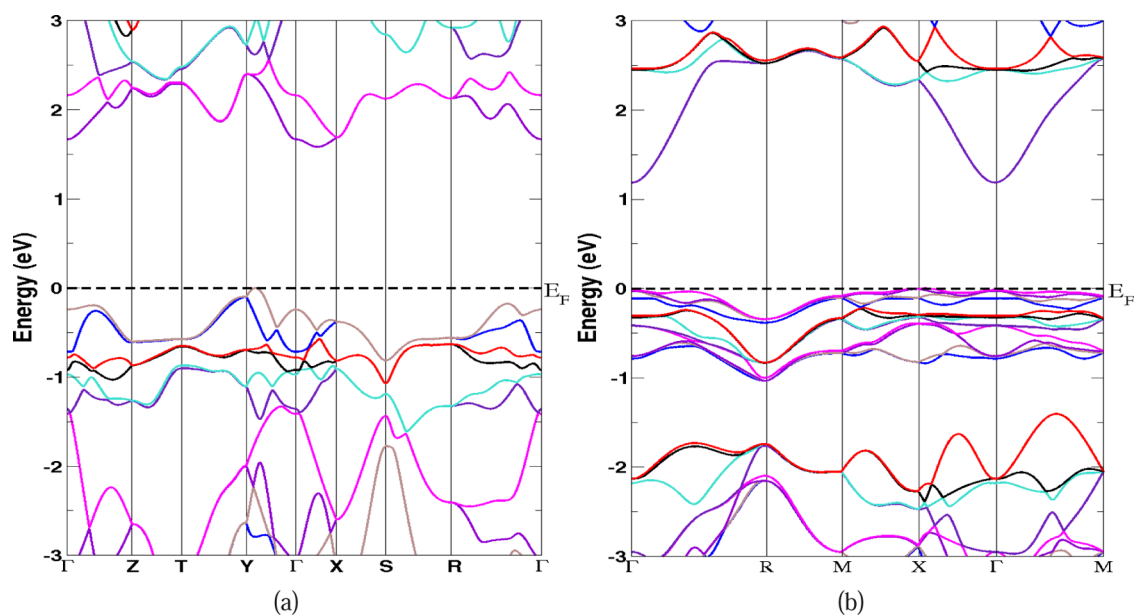


Figure 7. Band structure of (a) Marcasite and (b) Pyrite along the high-symmetry directions of the Brillouin zone.

Table 4. Calculated Effective Mass of the Marcasite and Pyrite in Some Selected Directions of the Brillouin Zone^a

	direction	valence band	conduction band
marcasite	Γ-X	0.118	0.490
	Γ-Y	0.081	0.058
	Γ-Z	0.062	0.099
pyrite	Γ-X	0.512	0.019
	Γ-M	0.656	0.116
	Γ-R	0.096	0.033

^a Values are given in the units of electron rest mass.

The calculated density of states (DOS) along with the I-projected DOS for both structures are shown in Figure 8a,b. In Figure 8b, it is clearly seen that there is a sudden increase in the DOS at the VBM (E_F), and this is also quite evident from the low dispersion seen in the band structure (Figure 7b). In the case of marcasite (Figure 8a) we find an increase in the DOS of the valence band up to -0.2 eV, then it dips a little near -0.2 eV and then increases again. We find a similar increasing trend in the DOS in the case of the conduction band for both

structures with a small variation in the marcasite. It is also evident from the above band structure and DOS that p-type doping is more favorable than n-type doping for obtaining better thermoelectric properties. Optimized doping level and transport properties are discussed in the next section.

4.2. Thermoelectric Properties. The recent experimental study of Xu et al.⁸⁰ reveals that natural minerals are good candidate materials for achieving high thermoelectric efficiency. In view of this, we have attempted to calculate the thermoelectric properties of both marcasite and pyrite phases of FeS_2 . To this end, we have calculated the thermopower and electrical conductivity/scattering time (σ/τ) as a function of carrier concentration and temperature using the Boltzmann transport equation approach as implemented in the BOLTZ-TRAP⁵⁴ code. These properties were calculated at ambient pressure for the marcasite phase and at high pressure for the pyrite phase. The results are discussed below.

The thermopower plays a vital role in deciding the performance of the thermoelectric material because of the direct proportionality of the figure of merit to the square of the

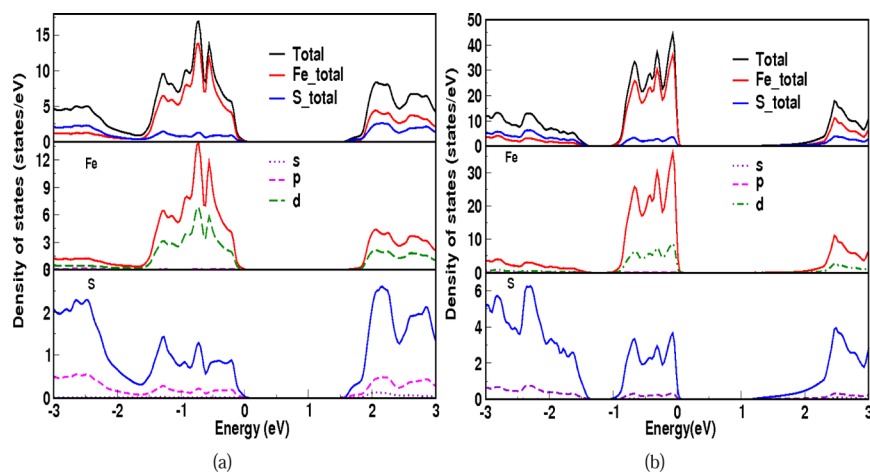


Figure 8. Density of states of (a) Marcasite and (b) Pyrite.

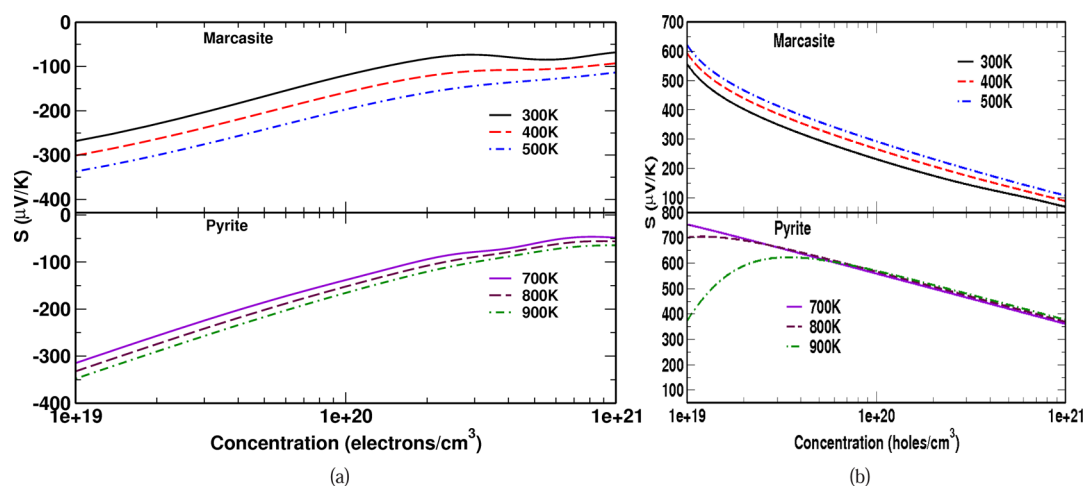


Figure 9. Thermopower variation of marcasite and pyrite with (a) Electron concentration and (b) Hole concentration.

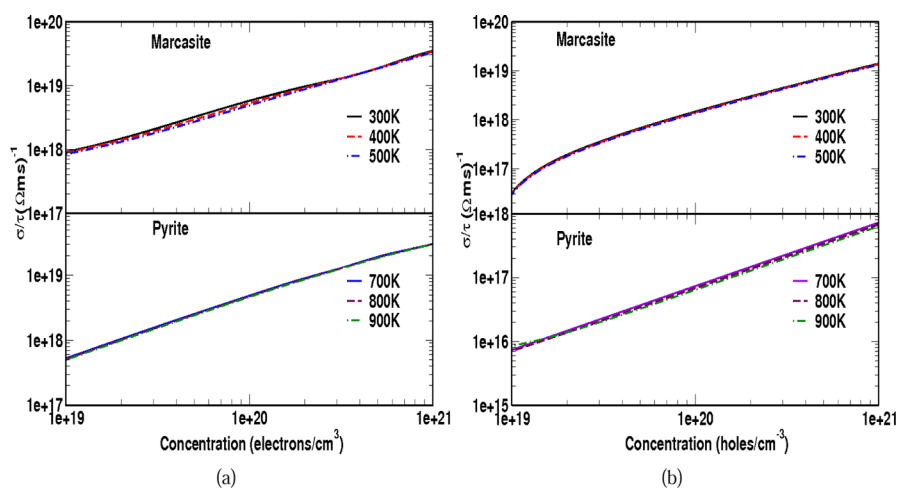


Figure 10. Electrical conductivity variation of marcasite and pyrite with (a) Electron concentration (b) Hole concentration.

thermopower ($ZT = (S^2\sigma T)/\kappa$). The thermopower calculated using the electronic structure data depends on the carrier concentration and temperature. In view of the constant scattering time approximation that is employed, energy dependence of τ is ignored. The calculated thermopower as a function of hole and electron concentrations at different temperatures are shown in Figure 9a,b. Here we have given the results for 300, 400, and 500 K for marcasite and 700, 800, and 900 K for pyrite, as marcasite is reported to be stable only below 573 K (300 °C), found to exist in a mixed state between 573–673 K (300–400 °C), and completely transformed to pyrite above 673 K (400 °C).^{3,81–84} We observe the thermopower increases with decreasing carrier concentration for both electron and hole doping, which implies the absence of bipolar conduction in the optimum concentration region. At low carrier concentrations (hole concentration of $1 \times 10^{19} \text{ cm}^{-3}$ at 900 K for pyrite), we can see a decrease in the thermopower, which indicates the onset of bipolar conduction in those regions. We also found the Pisarenko behavior (i.e., logarithmic variation) in the thermopower in the range of 10^{19} – 10^{21} cm^{-3} , which is an optimum working region for any good thermoelectric material. In this region, we find the thermopower of marcasite with a hole concentration of $1 \times 10^{19} \text{ cm}^{-3}$ to vary between 550–610 $\mu\text{V/K}$ for the temperature range 300–500 K. In the case of pyrite, the thermopower is higher, $\sim 750 \mu\text{V/K}$ up

to ~ 800 K, followed by a reduction at ~ 900 K due to the bipolar conduction. The difference between the thermopower values of marcasite and pyrite may be due to differences in effective masses of the carriers near the Fermi level of both structures (see Figure 7a,b). Hole doping leads to larger thermopower as compared to electron doping in both structures. The computed range of thermopower is in good agreement with the earlier experimental investigation of Maria Telkes⁸⁵ for both structures. This indicates that the marcasite and pyrite phases of FeS_2 are good thermoelectric materials with both hole and electron doping, but hole doping is preferred over electron doping. (As discussed above, this is also evident from Figure 8b.) In addition, we can also see that marcasite is favorable for low-temperature (up to 500 K) thermoelectric applications and pyrite is favorable for high-temperature (up to 900 K) thermoelectric applications.

The other important factor that influences the thermoelectric figure of merit is the electrical conductivity σ . While σ/τ is an intrinsic property of any material, the relaxation time τ also depends on nuances of material preparation. Therefore, we first consider variation of σ/τ with carrier concentration and temperature. Results of our calculation of σ/τ , as a function of both the electron and hole concentrations for both structures, are shown in Figure 10a,b. We found that there is no significant change in σ/τ with temperature in the

temperature range of interest when the carrier concentration is varied from 1×10^{19} to 1×10^{21} for both structures. We also observe that σ/τ varies from 1×10^{18} to 3×10^{19} ($\Omega \text{ m s}$)⁻¹ for marcasite and from 6×10^{17} to 3×10^{19} ($\Omega \text{ m s}$)⁻¹ for pyrite for the optimum hole concentration at the investigated temperatures. Because no general method exists to calculate microstructure-dependent relaxation times of electrons, we are not in a position to calculate $\sigma(T)$ from first principles. However, we have attempted to estimate the relaxation times of electrons at a fixed temperature and carrier concentration of the pyrite phase from the limited experimental data available on naturally occurring pyrite.⁸⁶ We have then used the same relaxation time for the marcasite structure because these two polymorphic phases are closely related. For the naturally occurring pyrite with an electron concentration of $3.3 \times 10^{18} \text{ cm}^{-3}$, the resistivity and thermal conductivity were found to be on the order of $2.17 \times 10^3 \Omega^{-1} \text{ m}^{-1}$ and $24.89 \text{ W m}^{-1} \text{ K}^{-1}$, respectively, at 578 K.⁸⁶ The corresponding relaxation time τ is estimated to be $101.1 \times 10^{-14} \text{ s}$; the computed resistivity matches the experimental value. Using this relaxation time, σ is calculated for various carrier concentrations. The value of ZT thus computed is found to be 0.32 for a concentration of 3×10^{19} at 700 K. Similarly, we found a ZT value of 0.14 for marcasite at 300 K. The value of ZT can be increased further by reducing the thermal conductivity by resorting to a nanostructuring technique^{87,88} as well as by improving σ by using phase-pure materials. Our theoretical calculations provide the guidelines for further experimental investigation in this regard.

5. CONCLUSION

In summary, we have reported a theoretical description of the structural transition of the natural mineral FeS₂. From this study, we conclude that the ground state of FeS₂ is the marcasite structure under ambient conditions and it transforms to the pyrite structure at high pressures. The calculated structural properties such as lattice parameters, internal coordinates of sulfur atoms, bond lengths, and bulk modulus at ambient conditions are in good agreement with available experimental data and other theoretical reports. We have also predicted the single-crystal and polycrystalline elastic properties and confirm that marcasite FeS₂ is mechanically stable at ambient conditions. Our calculations using pressure coefficients of three lattice parameters and single-crystal elastic constants confirmed that the marcasite phase is least compressible along the *b*-axis. Furthermore, the dynamic stability of marcasite FeS₂ is studied by phonon dispersion, and the calculated zone-centered frequencies at ambient and high pressure are in good agreement with earlier experimental and theoretical results. It is interesting to note that the calculated zone-centered frequencies and the phonon dispersion up to 5 GPa along different directions do not show any softening under pressure, reflecting the dynamic stability of marcasite FeS₂ up to 5 GPa. A discussion of the marcasite-to-pyrite structural transition is presented based on a detailed comparison of the geometry and energetics of the two structures. We have also calculated the electronic band gap using semilocal exchange–correlation functional TB-mBJ and found that both polymorphic structures are indirect band gap semiconductors. Finally, we have calculated thermoelectric properties and find that the thermopower for the high-pressure phase is relatively higher than that for the ambient phase. We also predict that marcasite can be used for low-temperature thermoelectric applications, whereas pyrite can be used for the high-temperature applications. We

hope that our work on the transport properties will further stimulate the experimentalists for a detailed study of the thermoelectric properties of this interesting mineral.

AUTHOR INFORMATION

Corresponding Author

*E-mail: kanchana@iith.ac.in.

Notes

The authors declare no competing financial interest.

ACKNOWLEDGMENTS

Authors thank Dr. G. Parthasarathy, CSIR-NGRI for bringing interest towards the structural stability of natural marcasite. V.K.G and V.K. acknowledge IIT-Hyderabad for the computational facilities. S.A. and G.V. thank the Center for Modelling Simulation and Design-University of Hyderabad for providing computational facilities. V.K. thanks the Natural Science Foundation of China for a Research Fellowship for International Young Scientists under Grant 11250110051.

REFERENCES

- (1) Errandonea, D.; Santamaría-Perez, D.; Vegas, A.; Nuss, J.; Jansen, M.; Rodríguez-Hernandez, P.; Muñoz, A. Structural Stability of Fe₅Si₃ and Ni₂Si Studied by High-Pressure X-ray Diffraction and Ab Initio Total-Energy Calculations. *Phys. Rev. B* **2008**, *77*, 094113-1–094113-12.
- (2) Rieder, M.; Crelling, J. C.; Šustai, O.; Drábek, M.; Weiss, Z.; Klementová, M. Arsenic in Iron Disulfides in a Brown Coal from the North Bohemian Basin, Czech Republic. *Int. J. Coal Geol.* **2007**, *71*, 115–121.
- (3) Kjekshus, A.; Rakke, T. Compounds with Marcasite Type Crystal Structure. XI. High Temperature Studies of Chalcogenides. *Acta Chem. Scand. A* **1975**, *29*, 443–452.
- (4) Donohue, P. C.; Bither, T. A.; Young, H. S. High-pressure Synthesis of Pyrite-Type Nickel Diphosphide and Nickel Diarsenide. *Inorg. Chem.* **1968**, *7*, 998–1001.
- (5) Takizawa, H.; Uheda, K.; Endo, T. A New Ferromagnetic Polymorph of CrSb₂ Synthesized Under High Pressure. *J. Alloys Compd.* **1999**, *287*, 145–149.
- (6) Takizawa, H.; Yamashita, T.; Uheda, K.; Endo, T. High Pressure Crystal Chemistry of Transition Metal Diantimonides. *Phys. Status Solidi B* **2001**, *223*, 35–39.
- (7) Goodenough, J. B. Energy Bands in TX₂ Compounds with Pyrite, Marcasite, and Arsenopyrite Structures. *J. Solid State Chem.* **1972**, *5*, 144–152.
- (8) Hull, G. W.; Hulliger, F. CuSe₂, A Marcasite Type Superconductor. *Nature* **1968**, *220*, 257–258.
- (9) Gou, H.; Hou, L.; Zhang, J.; Sun, G.; Gao, F. Theoretical Hardness of PtN₂ with Pyrite Structure. *Appl. Phys. Lett.* **2006**, *89*, 141910-1–141910-3.
- (10) Vaughan, D. J.; Rosso, K. M. Chemical Bonding in Sulfide Minerals. *Rev. Mineral. Geochem.* **2006**, *61*, 231–264.
- (11) Dódy, I.; Pósfai, M.; Buseck, P. R. Structural Relationship between Pyrite and Marcasite. *Am. Mineral.* **1996**, *81*, 119–125.
- (12) Richards, R. P.; Clopton, E. L.; Jaszczak, J. A. Pyrite and Marcasite Intergrowths from Northern Illinois. *Mineral. Rec.* **1995**, *26*, 129–138.
- (13) Murphy, R.; Strongin, D. R. Surface Reactivity of Pyrite and Related Sulfides. *Surf. Sci. Rep.* **2009**, *64*, 1–45.
- (14) Ennaoui, A.; Fiechter, S.; Pettenkofer, Ch.; Alonso-Vante, N.; Büker, K.; Bronold, M.; Höpfner, Ch.; Tributsch, H. Iron Disulfide for Solar Energy Conversion. *Sol. Energy Mater. Sol. Cells* **1993**, *29*, 289–370.
- (15) Ferrer, I. J.; Nevskaya, D. M.; de las Heras, C.; Sánchez, C. About the Band Gap Nature of FeS₂ as Determined from Optical and

- Photoelectrochemical Measurements. *Solid State Commun.* **1990**, *74*, 913–916.
- (16) Wadia, C.; Alivisatos, A. P.; Kammen, D. M. Materials Availability Expands the Opportunity for Large-Scale Photovoltaics Deployment. *Environ. Sci. Technol.* **2009**, *43*, 2072–2077.
- (17) Wadia, C.; Wu, Y.; Gul, S.; Volkman, S. K.; Guo, J.; Alivisatos, A. P. Surfactant-Assisted Hydrothermal Synthesis of Single Phase Pyrite FeS₂ Nanocrystals. *Chem. Mater.* **2009**, *21*, 2568–2570.
- (18) Spagnoli, D.; Refson, K.; Wright, K.; Gale, J. D. Density Functional Theory Study of the Relative Stability of the Iron Disulfide Polymorphs Pyrite and Marcasite. *Phys. Rev. B* **2010**, *81*, 094106-1–094106-9.
- (19) Birkholz, M.; Fiechter, S.; Hartmann, A.; Tributsch, H. Sulfur Deficiency in Iron Pyrite (FeS_{2-x}) and its Consequences for Band-Structure Models. *Phys. Rev. B* **1991**, *43*, 11926–11936.
- (20) Bronold, M.; Pettenkofer, C.; Jaegermann, W. Surface Photovoltage Measurements on Pyrite (100) Cleavage Planes: Evidence for Electronic Bulk Defects. *J. Appl. Phys.* **1994**, *76*, 5800–5808.
- (21) von Oertzen, G. U.; Skinner, W. M.; Nesbitt, H. W. Ab Initio and X-ray Photoemission Spectroscopy Study of the Bulk and Surface Electronic Structure of Pyrite (100) with Implications for Reactivity. *Phys. Rev. B* **2005**, *72*, 235427-1–235427-10.
- (22) Abd El Halim, A. M.; Fiechter, S.; Tributsch, H. Control of Interfacial Barriers in n-type FeS₂ (Pyrite) by Electrodepositing Metals (Co, Cu) Forming Isostructural Disulfides. *Electrochim. Acta* **2002**, *47*, 2615–2623.
- (23) Oertel, J.; Ellmer, K.; Bohne, W.; Röhrich, J.; Tributsch, H. Growth of n-type Polycrystalline Pyrite (FeS₂) Films by Metalorganic Chemical Vapour Deposition and their Electrical Characterization. *J. Cryst. Growth* **1999**, *198–199*, 1205–1210.
- (24) Mamiya, K.; Mizokawa, T.; Fujimori, A.; Takahashi, H.; Mōri, N.; Miyadai, T.; Suga, S.; Chandrasekharan, N.; Krishnakumar, S. R.; Sarma, D. D. Photoemission Study of Pyrite-type Transition-metal Chalcogenides MS_{2-x}Se_x (M=Fe,Co,Ni). *Phys. B* **1997**, *237–238*, 390–391.
- (25) Jagadeesh, M. S.; Seehra, M. S. Electrical Resistivity and Band Gap of Marcasite (FeS₂). *Phys. Lett. A* **1980**, *80A*, 59–61.
- (26) Lutz, H. D.; Müller, B. Lattice Vibration Spectra. LXVIII. Single-Crystal Raman Spectra of Marcasite-Type Iron Chalcogenides and Pnictides, FeX₂ (X=S, Se, Te; P, As, Sb). *Phys. Chem. Miner.* **1991**, *18*, 265–268.
- (27) Sourisseau, C.; Cavagnat, R.; Fouassier, M. The Vibrational Properties and Valence Force Fields of FeS₂, RuS₂ Pyrites and FeS₂ Marcasite. *J. Phys. Chem. Solids* **1991**, *52*, 537–544.
- (28) Kleppe, A. K.; Jephcoat, A. P. High-Pressure Raman Spectroscopic Studies of FeS₂ Pyrite. *Mineral. Mag.* **2004**, *68*, 433–441.
- (29) Bühner, W.; Lafougère, E.; Lutz, H. Lattice Dynamics of Pyrite FeS₂ by Coherent Neutron Scattering. *J. Phys. Chem. Solids* **1993**, *54*, 1557–1565.
- (30) Sithole, H. M.; Ngoepe, P. E.; Wright, K. Atomistic Simulation of the Structure and Elastic Properties of Pyrite (FeS₂) as a Function of Pressure. *Phys. Chem. Miner.* **2003**, *30*, 615–619.
- (31) Bullett, D. W. Electronic Structure of 3d Pyrite- and Marcasite-type Sulphides. *J. Phys. C: Solid State Phys.* **1982**, *15*, 6163–6174.
- (32) Ahuja, R.; Eriksson, O.; Johansson, B. Electronic and Optical Properties of FeS₂ and CoS₂. *Philos. Mag. B* **1998**, *78*, 475–480.
- (33) Merkel, S.; Jephcoat, A. P.; Shu, J.; Mao, H.-K.; Gillet, P.; Hemley, R. J. Equation of State, Elasticity, and Shear Strength of Pyrite Under High Pressure. *Phys. Chem. Miner.* **2002**, *29*, 1–9.
- (34) Sun, R.; Chan, M. K. Y.; Ceder, G. First-Principles Electronic Structure and Relative Stability of Pyrite and Marcasite: Implications for Photovoltaic Performance. *Phys. Rev. B* **2011**, *83*, 23531-1–23531-12.
- (35) Bither, T. A.; Bouchard, R. J.; Cloud, W. H.; Donohue, P. C.; Siemons, W. J. Transition Metal Pyrite Dichalcogenides. High-Pressure Synthesis and Correlation of Properties. *Inorg. Chem.* **1968**, *7*, 2208–2220.
- (36) Parker, D.; Singh, D. J. First Principles Investigations of the Thermoelectric Behavior of Tin Sulfide. *J. Appl. Phys.* **2010**, *108*, 083712-1–083712-3.
- (37) Yan, Y. L.; Wang, Y. X. Electronic Structure and Thermoelectric Properties of In_{32-x}Ge_xO₄₈ (x = 0, 1, 2, and 3) at Low Temperature. *Appl. Phys. Lett.* **2010**, *97*, 252106-1–252106-3.
- (38) Baroni S.; Gironcoli S. D.; dal Corso A., et al. 2008, <http://www.pwscf.org>.
- (39) Perdew, J. P.; Burke, K.; Ernzerhof, M. Generalized Gradient Approximation Made Simple. *Phys. Rev. Lett.* **1996**, *77*, 3865–3868.
- (40) Monkhorst, H. J.; Pack, J. D. Special Points for Brillouin-Zone Integrations. *Phys. Rev. B* **1976**, *13*, 5188–5192.
- (41) Vanderbilt, D. Soft Self-Consistent Pseudopotentials in a Generalized Eigenvalue Formalism. *Phys. Rev. B* **1990**, *41*, 7892–7895.
- (42) Payne, M. C.; Teter, M. P.; Allan, D. C.; Arias, T. A.; Joannopoulos, J. D. Iterative Minimization Techniques for Ab Initio Total-energy Calculations: Molecular Dynamics and Conjugate Gradients. *Rev. Mod. Phys.* **1992**, *64*, 1045–1097.
- (43) Segall, M. D.; Lindan, P. J. D.; Probert, M. J.; Pickard, C. J.; Hasnip, P. J.; Clark, S. J.; Payne, M. C. First Principles Simulation: Ideas, Illustrations and the CASTEP Code. *J. Phys.: Cond. Matter* **2002**, *14*, 2717–2744.
- (44) Hill, R. The Elastic Behaviour of a Crystalline Aggregate. *Proc. Phys. Soc., Sect. A* **1952**, *65*, 349–354.
- (45) Ravindran, P.; Fast, L.; Korzhavyi, P. A.; Johansson, B.; Wills, J.; Eriksson, O. Density Functional Theory for Calculation of Elastic Properties of Orthorhombic Crystals: Application to TiSi₂. *J. Appl. Phys.* **1998**, *84*, 4891–4904.
- (46) Blaha, P.; Schwarz, K.; Madsen, G. K. H.; Kvasnicka, D.; Luitz, J. WIEN2k, An Augmented Plane Wave + Local Orbitals Program for Calculating Crystal Properties. <http://www.wien2k.at/>, Techn. Universität Wien, Austria.
- (47) Panchal, V.; Errandonea, D.; Segura, A.; Rodríguez-Hernandez, P.; Muñoz, A. The Electronic Structure of Zircon-Type Orthovanadates: Effects of High-Pressure and Cation Substitution. *J. Appl. Phys.* **2011**, *110*, 043723.
- (48) Tran, F.; Blaha, P. Accurate Band Gaps of Semiconductors and Insulators with a Semilocal Exchange–Correlation Potential. *Phys. Rev. Lett.* **2009**, *102*, 226401-1–226401-4.
- (49) Becke, A. D.; Johnson, E. R. A Simple Effective Potential for Exchange. *J. Chem. Phys.* **2006**, *124*, 221101-1–221101-4.
- (50) Koller, D.; Tran, F.; Blaha, P. Merits and Limits of the Modified Becke–Johnson Exchange Potential. *Phys. Rev. B* **2011**, *83*, 195134-1–195134-10.
- (51) Koller, D.; Tran, F.; Blaha, P. Improving the Modified Becke–Johnson Exchange Potential. *Phys. Rev. B* **2012**, *85*, 155109-1–155109-8.
- (52) Dixit, H.; Saniz, R.; Cottenier, S.; Lamoen, D.; Partoens, B. Electronic Structure of Transparent Oxides with the Tran–Blaha Modified Becke–Johnson Potential. *J. Phys.: Condens. Matter* **2012**, *24*, 205503-1–205503-19.
- (53) Hong, J. Band Gaps from the Tran–Blaha Modified Becke–Johnson Approach: A Systematic Investigation. *J. Chem. Phys.* **2013**, *138*, 134115-1–134115-7.
- (54) Madsen, G. K. H.; Singh, D. J. A Code for Calculating Band-Structure Dependent Quantities. *Comput. Phys. Commun.* **2006**, *175*, 67–71.
- (55) Scheidemantel, T. J.; Ambrosch-Draxl, C.; Thonhauser, T.; Badding, J. V.; Sofo, J. O. Transport Coefficients from First-Principles Calculations. *Phys. Rev. B* **2003**, *68*, 125210-1–125210-6.
- (56) Jodin, L.; Tobola, J.; Pecheur, P.; Scherrer, H.; Kaprzyk, S. Effect of Substitutions and Defects in Half-Heusler FeVSb Studied by Electron Transport Measurements and KKR–CPA Electronic Structure Calculations. *Phys. Rev. B* **2004**, *70*, 184207-1–184207-11.
- (57) Chaput, L.; Pêcheur, P.; Tobola, J.; Scherrer, H. Transport in Doped Skutterudites: Ab-initio Electronic Structure Calculations. *Phys. Rev. B* **2005**, *72*, 085126-1–085126-11.

- (58) Bilc, D. I.; Mahanti, S. D.; Kanatzidis, M. G. Electronic Transport Properties of PbTe and AgPb_mSbTe_{2+m} Systems. *Phys. Rev. B* **2006**, *74*, 125202-1–125202-12.
- (59) Ziman, J. M. *Electrons and Phonons: Theory of Transport Phenomena in Solids*; Oxford University Press: London, UK, 1960.
- (60) Nag, B. R. *Electron Transport in Compound Semiconductors*; Springer-Verlag: Berlin, 1980.
- (61) Singh, D. J. Thermopower of SnTe from Boltzmann Transport Calculations. *Func. Mat. Lett.* **2010**, *3*, 223–226.
- (62) Khuong, P. O.; Singh, D. J.; Ping, Wu. Analysis of the Thermoelectric Properties of n-type ZnO. *Phys. Rev. B* **2011**, *83*, 115110-1–115110-5.
- (63) Parker, D.; Singh, D. J. Thermoelectric Properties of AgGaTe₂ and Related Chalcopyrite Structure Materials. *Phys. Rev. B* **2012**, *85*, 125209-1–125209-7.
- (64) Singh, D. J.; Mazin, I. I. Calculated Thermoelectric Properties of La-filled Skutterudites. *Phys. Rev. B* **1997**, *56*, R1650–R1653.
- (65) Parker, D.; Singh, D. J. High-Temperature Thermoelectric Performance of Heavily Doped PbSe. *Phys. Rev. B* **2010**, *82*, 035204-1–035204-5.
- (66) Zhang, L.; Du, M.-H.; Singh, D. J. Zintl-phase Compounds with SnSb₄ Tetrahedral Anions: Electronic Structure and Thermoelectric Properties. *Phys. Rev. B* **2010**, *81*, 075117-1–075117-8.
- (67) Buerger, M. J. *Zeitschrift Fuer Kristallographie, Kristallgeometrie, Kristallphysik, Kristallchemie* **1937**, *97A*, 504 (Pearson handbook of crystallographic data).
- (68) Chattopadhyay, T.; von Schnering, H. G. High Pressure X-ray Diffraction Study on p-FeS₂, m-FeS₂ and MnS₂ to 340 kbar: A Possible High Spin–low Spin Transition in MnS₂. *J. Phys. Chem. Solids* **1985**, *46*, 113–116.
- (69) Sithole, H. M.; Nguyen-Manh, D.; Pettifor, D. G.; Ngoepe, P. E. Internal Relaxation, Band Gaps and Elastic Constant Calculations of FeS₂. *Mol. Simul.* **1999**, *22*, 31–37.
- (70) Born, M.; Huang, K. *Dynamical Theory of Crystal Lattices*; Oxford University Press: Oxford, U.K., 1988.
- (71) Gonze, X. First-principles Responses of Solids to Atomic Displacements and Homogeneous Electric Fields: Implementation of a Conjugate-gradient Algorithm. *Phys. Rev. B* **1997**, *55*, 10337–10354.
- (72) Kanchana, V.; Gudelli, V. K.; Vaitheeswaran, G.; Appalakondaiah, S.; Parthasarathy, G. Pressure Induced Phase Transition in Natural FeS₂: A Combined Experimental and Theoretical Study. Presented at 57th DAE–SSP Symposium, IIT Bombay, December 3–7, 2012.
- (73) Hulliger, F.; Mooser, E. Semiconductivity in Pyrite, Marcasite and Arsenopyrite Phases. *J. Phys. Chem. Solids* **1965**, *26*, 429–433.
- (74) Opahle, I.; Koepf, K.; Eschrig, H. Full-potential Band-structure Calculation of Iron Pyrite. *Phys. Rev. B* **1999**, *60*, 14035–14041.
- (75) Will, G.; Lauterjung, J.; Schmitz, H.; Hinze, E. *High Pressure in Science and Technology (Materials Research Society Symp. Proc. Homan, C, MacCrone, R. K., Whalley, E., Eds; Elsevier: New York, 1984, Vol 22, p 49.*
- (76) Ahrens, T. J.; Jeanloz, R. Pyrite: Shock Compression, Isentropic Release, and Composition of the Earth's Core. *J. Geophys. Res.* **1987**, *29*, 10363–10375.
- (77) Schlegel, A.; Wachter, P. Optical Properties, Phonons and Electronic Structure of Iron Pyrite (FeS₂). *J. Phys. C: Solid State Phys.* **1976**, *9*, 3363–3369.
- (78) Hu, J.; Zhang, Y.; Law, M.; Wu, R. Increasing the Band Gap of Iron Pyrite by Alloying with Oxygen. *J. Am. Chem. Soc.* **2012**, *134*, 13216–13219.
- (79) Eyert, V.; Höck, K.-H.; Fiechter, S.; Tributsch, H. Electronic Structure of FeS₂: The Crucial Role of Electron-Lattice Interaction. *Phys. Rev. B* **1998**, *57*, 6350–6359.
- (80) Xu, L.; Morelli, D. T. Natural Mineral Tetrahedrite as a Direct Source of Thermoelectric Materials. *Phys. Chem. Chem. Phys.* **2013**, *15*, 5762–5766.
- (81) Fleet, M. E. Structural Aspects of the Marcasite–Pyrite Transformation. *Can. Mineral.* **1970**, *10*, 225–231.
- (82) Grønvold, F.; Westrum, E. F., Jr. Heat Capacities of Iron Disulfides Thermodynamics of Marcasite from 5 to 700 K, Pyrite from 300 to 780 K, and the Transformation of Marcasite to Pyrite. *J. Chem. Thermodyn.* **1976**, *8*, 1039–1048.
- (83) Murowchick, J. B.; Barnes, H. L. Marcasite Precipitation from Hydrothermal Solutions. *Geochim. Cosmochim. Acta* **1986**, *50*, 2615–2629.
- (84) Lennie, A. R.; Vaughan, D. J. Kinetics of the Marcasite–Pyrite Transformation: An Infrared Spectroscopic Study. *Am. Mineral.* **1992**, *77*, 1166–1171.
- (85) Telkes, M. Thermoelectric Power and Electrical Resistivity of Minerals. *Am. Miner.* **1950**, *35*, 536–555.
- (86) Kato, K.; Okamoto, Y.; Morimoto, J.; Miyakawa, T. The Thermoelectric Properties of FeS₂. *J. Mater. Sci. Lett.* **1997**, *16*, 914–916.
- (87) Venkatasubramanian, R.; Siivola, E.; Colpitts, T.; O'Quinn, B. Thin-Film Thermoelectric Devices with High Room-Temperature Figures of Merit. *Nature* **2001**, *413*, 597–602.
- (88) Harman, T. C.; Taylor, P. J.; Walsh, M. P.; LaForge, B. E. Quantum Dot Superlattice Thermoelectric Materials and Devices. *Science* **2002**, *297*, 2229–2232.